Determining the Absolute Abundances of Natural Radioactive Elements on the Lunar Surface by the Kaguya Gamma-ray Spectrometer

S. Kobayashi · N. Hasebe · E. Shibamura · O. Okudaira · M. Kobayashi · N. Yamashita · Y. Karouji · M. Hareyama · K. Hayatsu · C. d'Uston · S. Maurice · O. Gasnault · O. Forni · B. Diez · R.C. Reedy · K.J. Kim

Abstract The Kaguya gamma-ray spectrometer (KGRS) has great potential to precisely determine the absolute abundances of natural radioactive elements K, Th and U on the lunar surface because of its excellent spectroscopic performance. In order to achieve the best performance of the KGRS, it is important to know the spatial response function (SRF) that describes the directional sensitivity of the KGRS. The SRF is derived by a series of Monte Carlo simulations of gamma-ray transport in the sensor of the KGRS using the full-fledged simulation model of the KGRS, and is studied in detail. In this paper, the method for deriving absolute abundance of natural radioactive elements based on the SRF is described for the

S. Kobayashi (✉) · N. Hasebe · O. Okudaira · N. Yamashita · Y. Karouji · M. Hareyama · K. Hayatsu
Research Institute for Science and Engineering, Waseda University, 3-4-1 Okubo Shinjuku-ku, Tokyo 169-8555, Japan
e-mail: shingo@planeta.sci.isas.jaxa.jp

S. Kobayashi · M. Hareyama
Japan Aerospace Exploration Agency, 3-1-1 Yoshinodai Chuo-ku, Sagamihara, Kanagawa 252-5210, Japan

E. Shibamura
School of Health and Social Services, Saitama Prefectural University, 820 Sannomiya, Koshigaya, Saitama 343-8540, Japan

M. Kobayashi
Planetary Exploration Research Center, Chiba Institute of Technology, 2-17-1 Tsudanuma, Narashino, Chiba 275-0016, Japan

N. Yamashita · C. d'Uston · S. Maurice · O. Gasnault · O. Forni · B. Diez
Centre d'Etude Spatiale des Rayonnements, Université de Toulouse, CNRS, 9 avenue Colonel Roche, 31400 Toulouse, France

R.C. Reedy
Planetary Science Institute, 152 Monte Rey Drive, Los Alamos, NM 87544, USA

K.J. Kim
Korea Institute of Geoscience & Mineral Resources (KIGAM), 92 Gwahang-no, Yuseong-gu, Daejeon 305-350, Korea

analysis of KGRS data, which is also applicable to any gamma-ray remote sensings. In the preliminary analysis of KGRS data, we determined the absolute abundances of K and Th on the lunar surface without using any previous knowledge of chemical information gained from Apollo samples, lunar meteorites and/or previous lunar remote sensings. The results are compared with the previous measurements and the difference and the correspondence are discussed. Future detailed analysis of KGRS data will provide new and more precise maps of K, Th and U on the lunar surface.

Keywords Moon · SELENE (Kaguya) · Gamma-ray spectrometer · Spatial response function · Natural radioactive elements · K · Th · U

Abbreviations

AGRS   Apollo Gamma-Ray Spectrometer
BGO   Bismuth Germanate
FOV   Field Of View
FWHM   Full Width of Half Maximum
KGRS   Kaguya Gamma-Ray Spectrometer
KGRD   Kaguya Gamma-Ray Detector
LPGRS   Lunar Prospector Gamma-Ray Spectrometer
PMT   Photo Multiplier Tube
SRF   Spatial Response Function

1 Introduction

The Kaguya Gamma-Ray Spectrometer (KGRS) remotely measured gamma rays that originated from the Moon in order to determine the abundance of chemical elements on the lunar surface. One of the most outstanding features of the KGRS is excellent energy resolution due to the employment of a high-purity germanium detector cooled by a Stirling cryocooler (Kobayashi et al. 2005; Kobayashi et al. 2005; Hasebe et al. 2008). The energy resolution of the KGRS for 1.333 MeV gamma rays during the mission, which changed due to the radiation damage to the KGRS sensor and the annealing operation to recover from it, was 10 to 15 times better than that of Lunar Prospector gamma-ray spectrometer (LPGRS, Lawrence et al. 1998) and was 8 to 13 times better than that of Apollo gamma-ray spectrometers (AGRS, Metzger et al. 1973). A new record of energy resolution for in-flight data in lunar gamma-ray spectroscopy has been achieved.

Characteristic gamma rays of K, Th, U, O, Mg, Al, Si, Ca, Ti and Fe in the energy spectra obtained by the KGRS are clearly separated due to the excellent energy resolution (Hasebe et al. 2009). These peak identifications are very important in terms of quantitative measurement. They enable an accurate and confident estimation of the count rate of a characteristic gamma-ray peak, which is often obscured by background of gamma-ray continuum and interference of the other peaks near it. Noticeably, the accurate estimation of the count rate by the KGRS makes it possible for us to precisely determine the absolute abundance of natural radioactive elements (K, Th and U) on the lunar surface without the help of ground truths, as is discussed in this paper. Therefore, the determination of the absolute abundance is one of the significant missions imposed on the KGRS, after the LPGRS that showed the dichotomy of Th distribution on the lunar surface and released global maps of some chemical elements (Lawrence et al. 1998; Feldman et al. 2004; Prettyman et al. 2006).

The spatial response function (SRF) related to the directional sensitivity of the KGRS is needed for the determination of the absolute abundances of K, Th and U. The SRF generally

plays a significant role in gamma-ray remote sensing, since it is used for the estimation of spatial resolution (e.g., Reedy et al. 1973), the smoothing of statistically varied gamma-ray intensity maps (e.g., Lawrence et al. 2003), and the gamma-ray image restoration of spatial deconvolution analysis (e.g., Haines et al. 1978; Lawrence et al. 2007) as well as the determination of the absolute abundances. However, there is a problem in deriving the SRF of a gamma-ray spectrometer. The derivation of the SRF demands a complete set of detection efficiencies of the sensor for a gamma ray incident from all directions. It is often difficult to gather all of the efficiencies experimentally because of the time limitation for the preflight calibration. High penetrability of gamma rays through material makes the sensor more or less sensitive to all directions and makes the situation more difficult. In addition, the anisotropic shape of the sensor and the asymmetric arrangement of surrounding components complicate the directional sensitivity to gamma rays. This problem is crucial and common to all gamma-ray spectrometers for planetary gamma-ray remote sensing missions that are finished, in cruise, and under development (e.g., MESSENGER, Goldsten et al. 2007; Bepi-Colombo, Mitrofanov et al. 2010; NEAR, Goldsten 1998; Mars Odyssey, Boynton et al. 2004; DAWN, Prettyman et al. 2003), and the KGRS is no exception.

An approach to this problem is a spherical approximation of the sensor, i.e., the assumption of isotropic response to gamma rays, but it degrades the excellent ability of the KGRS to determine absolute abundance. In order to construct the SRF of the KGRS, we have developed a three-dimensional model of the KGRS that is used to accurately calculate the detection efficiencies for gamma rays from any incident direction, based on the Monte Carlo simulation code for the transport of particles in material, Geant4 (Agostinelli et al. 2003). The detection efficiencies of the KGRS for incidents from various directions are calculated by a series of Monte Carlo simulations, and thus the SRF for the KGRS are derived. The relationship between the anisotropic sensitivity of the KGRS and the asymmetric arrangement of components around the sensor can be well understood from the results of these simulations.

The purpose of this paper is to obtain the KGRS's SRF and to construct a method for determining the absolute abundances of K, Th and U from the data obtained by the KGRS. The abundance of natural radioactive elements is important because it provides constraints to interesting questions about the origin and evolution of the Moon (e.g., Gillis et al. 2004; Taylor et al. 2006) and clues about the formation and lithology of some local regions (e.g., Hagerty et al. 2009). We have determined the preliminary abundances of K and Th on the lunar surface based on the method presented here. The KGRS is also able to determine the abundances of major elements (O, Mg, Al, Si, Ca, Ti and Fe), but we need additionally the excitation rates of the target nuclei as a function of depth in the lunar subsurface in the analysis of major elements. This issue is related to the interactions of cosmic rays within the lunar surface material (e.g., Reedy et al. 1973), and a study of the transport of neutrons produced by the cosmic rays in the lunar subsurface is necessary. The determination of the abundances of the major elements is outside the scope of this paper and will be discussed elsewhere in the future.

## 2 The KGRS and Its Model Used in Monte Carlo Calculation

The configuration of the components around the KGRS sensor characterizes the response to gamma rays from the lunar surface. In this section, the configuration of the KGRS sensor is described and the simulation model that approximates the KGRS sensor is discussed. The simulation model is evaluated by comparing detection efficiencies of the KGRS obtained by

the simulation with experimentally measured ones. The simulation model is used to calculate the photopeak efficiency and solid angles of the KGRS, both of which are required by the calculation of the SRF.

2.1 Configuration of the KGRS

The KGRS is composed of three subsystems: the gamma-ray detector (GRD), the Cooler Driving Unit (CDU) and the Gamma-ray and Particle detector Electronics (GPE). Here, only the configuration of the Kaguya GRD (KGRD), which consists of the sensor and the cooling system, is mentioned because it is of particular importance in learning the KGRS response to gamma rays from the lunar surface. For details on the entire KGRS instrument, refer to Hasebe et al. (2008).

Schematic drawings of KGRD and a definition of the coordinate system fixed to the KGRD are shown in Fig. 1. The KGRD is installed on the lunar side of the Kaguya spacecraft and is covered by multi-layer insulators to moderate thermal stress due to the lunar albedo, which is not shown in Fig. 1. The KGRD consists of germanium crystal, two kinds of scintillator coupled with three photomultiplier tubes (PMTs) for the rejection of backgrounds, a Stirling cryocooler, pre-amplifiers, and high-voltage power supplies. The cryocooler consists of a compressor, a displacer and a radiator, as can be seen in Fig. 1a. The Ge crystal has a closed-end coaxial shape (a cylinder of 65 mm dia. × 77 mm length with a hole of 10 mm dia. and 67 mm depth), and is encapsulated by an aluminum canister. The Ge crystal is designed with its axis not to the nadir but parallel to the lunar surface. This maximizes the detection efficiency of the Ge detector for the lunar gamma rays and the rejection of background from the spacecraft body by the anti-coincidence scintillation detectors (explained below) under the limitation of the total weight of the KGRD system. As a result, the solid angle subtended by the Ge crystal is changed, depending on the incident direction of lunar gamma rays. This leads to a weak anisotropic response of the KGRD. The bismuth germanate (BGO) scintillator shields gamma rays from all the sides of the Ge crystal except
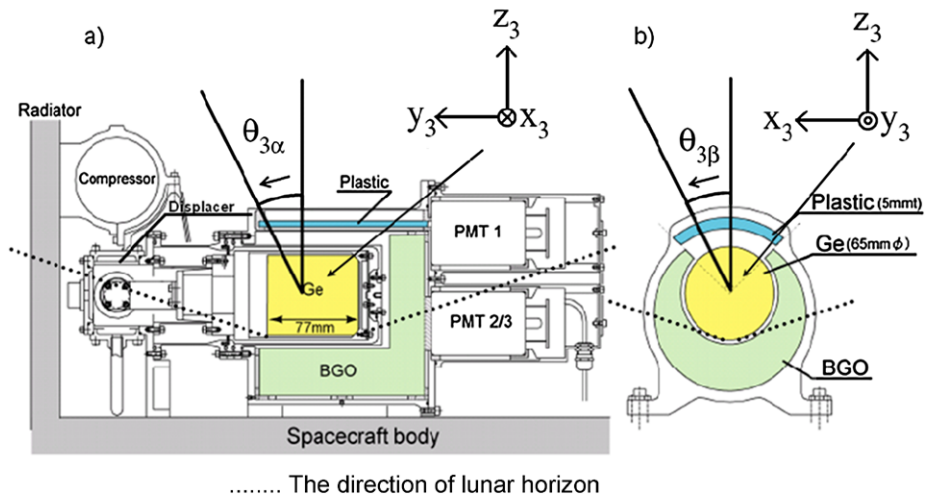
Fig. 1 Schematic drawings of KGRS and definitions of a coordinate system and symbols. *Dotted lines* show FOV determined by the lunar horizon when KGRS is operated at an altitude of 100 km. The origin of the coordinate system (x_3, y_3, z_3) is fixed at the center of the aluminum canister

for the sides facing the Moon and the radiator. The thickness of the BGO varies from 10 to 40 mm and is the thickest on the spacecraft side, effectively shielding the Ge crystal from the spacecraft's intensive background gamma rays. The BGO has a high density (7.1 g/cm^3) and a large cross section for gamma rays. Thus a significant difference in detection efficiency between the lunar gamma rays incident from the radiator side and from the PMT side is expected. The plastic scintillator (Plastic) is installed on the lunar side of the Ge detector. Most lunar gamma rays penetrate it without any interactions before entering the Ge crystal, whereas high energy charged particles deposit energy in Plastic and they are detected. The BGO and the Plastic are used as anti-coincidence detectors for the Ge detector to suppress the Compton continuum background and for the rejection of backgrounds due to cosmic rays.

Kaguya is a 3-axis stabilized satellite and $+z_3$-axis is oriented toward the center of the Moon at any time during the normal operation, thus the incident directions of lunar gamma rays are well determined if the altitude of the spacecraft is constant. The field of view (FOV) determined by the lunar horizon during the observation at an altitude of 100 km is drawn in Fig. 1 with dotted lines. The aluminum canister, BGO, Plastic, PMTs, radiator and compressor, etc., are located in the FOV and cause an anisotropic response of the KGRD. It is crucial to estimate the influence of the surrounding materials on the KGRS observation.

2.2 Model of the KGRD by Geant4

A three-dimensional model of the KGRD has been developed using a Geant4 toolkit (Agostinelli et al. 2003) for the calculations of solid angles and photopeak efficiencies of the KGRD. Geant4 is a simulation toolkit for the calculation of the passage of particles through matter. We adopted Geant4 for the modeling of the KGRD because it includes powerful libraries able to model a detector with a complex shape.

Three models with different levels of approximations for the KGRD are constructed using Geant4. In the most primitive model, the KGRD is approximated as a sphere of germanium with the same volume of the Ge crystal (sphere). This model does not include any other components. In the second model (level 1), only the three components of the Ge detector, BGO and Plastic are implemented with true geometries and materials. In the current final model (level 2), shown in Fig. 2, we takes into account the Ge detector, the aluminum canister, Plastic, BGO, PMTs, the cooling system of the displacer, the compressor and the

Fig. 2 Level 2 model of KGRS used by the calculation of the detection efficiency and the solid angle
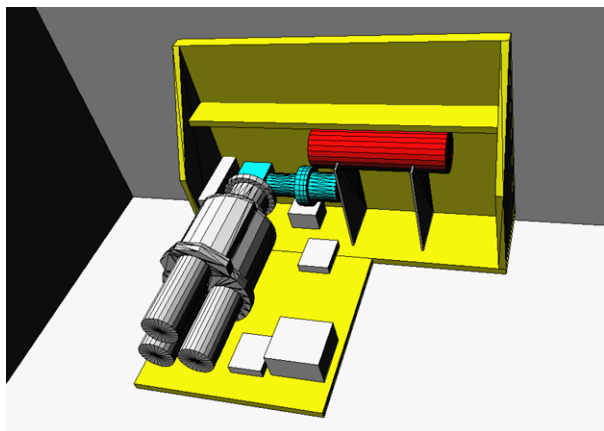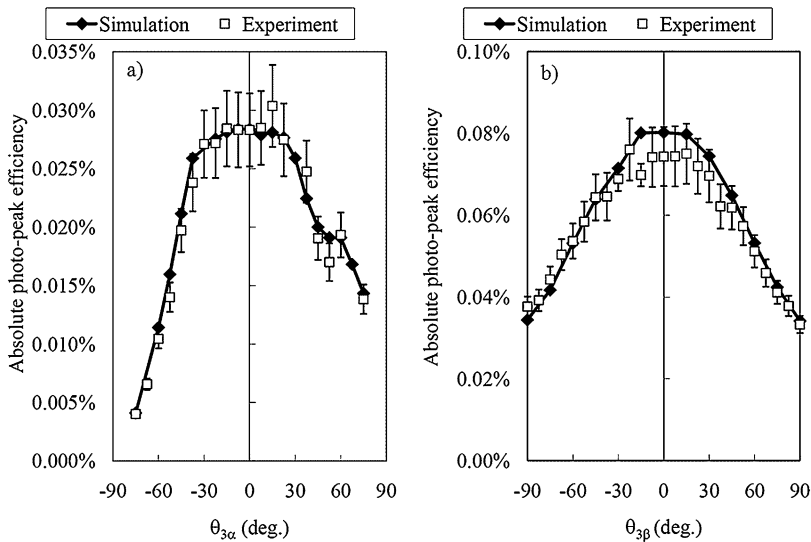
Fig. 3 Absolute photopeak efficiencies for 1.333 MeV from ^{60}Co obtained by the simulation and the preflight experiment made in May 2003

radiator, the boxes for electronics and the base plate. The Ge detector, the aluminum canister, Plastic, BGO and the aluminum case for the detectors are modeled in level 2 as closely as possible, because the rough modeling of the parts that are very near the Ge crystal and at the center of the FOV could result in a large systematic error. Alternatively, the PMTs, cooling system and electronics boxes are approximated with similar shapes and weights filled with aluminum (titanium for the supporter of the compressor), since they are relatively far from the Ge crystal, and their true geometries and materials of them are too complicated. Although the level 2 model does not include the spacecraft body or the instruments next to the KGRD, they are almost out of the FOV and give negligibly small effects on the calculations.

2.3 Experiments vs. Simulations

Before the launch, the photopeak efficiencies of the KGRD were measured using standard sources of ^{60}Co and ^{133}Ba. In the preflight experiment in May 2003, the photopeak efficiencies of the KGRD for about 100 incident directions were measured by using a ^{60}Co source. Here, two experiments in 2003 are shown. In the first experiment, the ^{60}Co source was placed at 50 cm from the center of the canister. Changing the position of the source on the $y_3 z_3$-plane that included the axis of the Ge crystal ($\theta_{3\alpha}$, see Fig. 1a), the absolute detection efficiencies were measured. The second experiment was almost the same as the first one, but the ^{60}Co source was placed at 30 cm from the center of the canister and the position of it was shifted on the $z_3 x_3$-plane (the positions of the ^{60}Co source are expressed by $\theta_{3\beta}$ in Fig. 1b). The absolute photopeak efficiencies are plotted in Fig. 3a and b as a function of $\theta_{3\alpha}$ and $\theta_{3\beta}$, respectively, with those calculated by Geant4 using the level 2 model. The consistency between the experiment and the simulation is fairly good.

   In the preflight measurement in Aug. 2006, the detection efficiencies of the KGRD were measured, fixing ^{133}Ba and ^{60}Co sources at the positions of $(x_3, y_3, z_3) = (-31.1$ mm, 2.0 mm, 268.0 mm) and $(x_3, y_3, z_3) = (-15.0$ mm, 22.0 mm, 189.5 mm), respectively. The differences of the detection efficiencies between the experiment and the calculation

Fig. 4 The difference of the photopeak efficiencies between the experiment (Exp.) made in May 2003 and August 2006 and the simulation by using level 2 model (Sim.). The plots for 1.173 and 1.333 MeV are slightly moved horizontally to better see the error bars
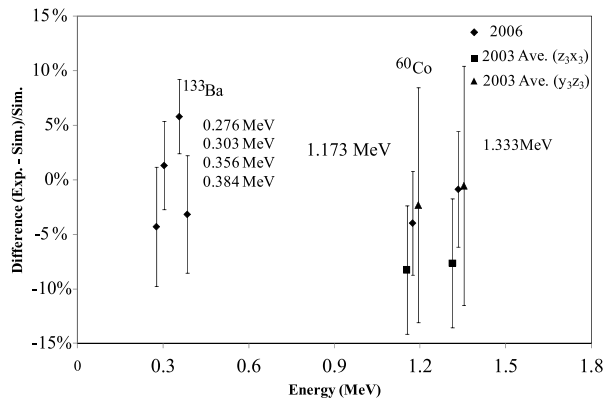
are shown in Fig. 4 along with the result of the experiment in 2003. If the data points in Fig. 4 are assumed to be randomly distributed, the weighted average of the difference is $(1.5 \pm 0.1)\%$, $(-5.3 \pm 0.2)\%$ and $(-3.5 \pm 0.2)\%$ for 0.276 to 0.384 MeV, 1.173 MeV and 1.333 MeV, respectively. The differences with the negative sign between the experiment and the simulation can be likely attributed to the incomplete collection of charges induced by gamma-rays in the detector (Moss and Streetman 1990). If the maximum and the minimum of the data points are adopted as the difference, the data points are within -8% to $+6\%$. Therefore, we conclude that the systematic error of the level 2 model is $< \pm 8\%$ as a conservative estimate.

3 The Method for Deriving the Absolute Abundance of Natural Radioactive Elements

In this section, we connect the directly measurable value by the KGRS, the count rate of a gamma-ray peak in the spectrum, to the abundance of a natural radioactive element in the lunar subsurface. The SRF plays the major role for this connection. The SRF is defined here, and the coefficient that converts the count rate to the absolute abundance is derived using the SRF. For example, the method to obtain K abundance in the lunar regolith from the observed count rate is given in this section.

3.1 Definition of Symbols and Coordinate Systems

In Fig. 5, the symbols h, R, and l represent the distance from the lunar surface to the center of the aluminum canister, the average radius of the Moon ($R = 1738$ km), and the distance from the center of the aluminum canister to an arbitrary parcel with an area of dS on the lunar surface, respectively. Origins of coordinate systems #1 and #3 are fixed at the center of the Moon and the center of the aluminum canister, respectively. Both Cartesian representation and polar representation are used to define a position, depending on the situation, and the coordinate system number is added as a subscript to coordinate variables for convenience. For example, the location of the parcel on the lunar surface is expressed by polar representation as (R, θ_1, φ_1) and (l, θ_3, φ_3) by systems of #1 and #3, respectively. In the coordinate system #3, the direction of x_3-, y_3-, and z_3-axis are definitely defined as shown in Fig. 1. The origin of #2 is set on the parcel, and the location of the aluminum canister is indicated by (l, θ_2, φ_2).

Fig. 5 Definitions of coordinate systems and symbols. Origins of the coordinate system of #1, #2, and #3 are located at the center of the Moon, an arbitrary point on the lunar surface in the detector's FOV, and the center of the aluminum canister, respectively
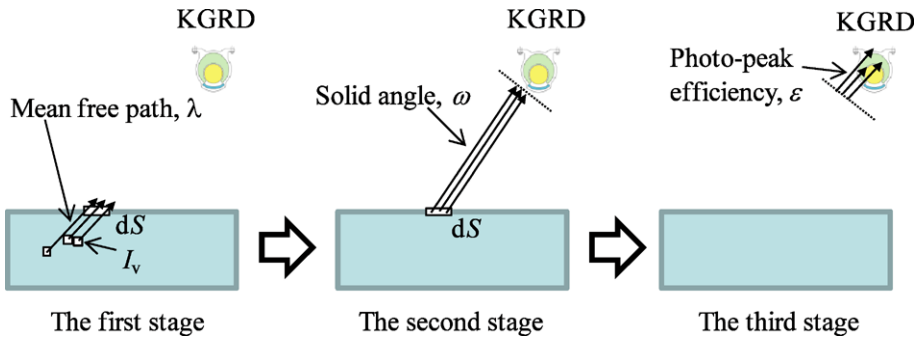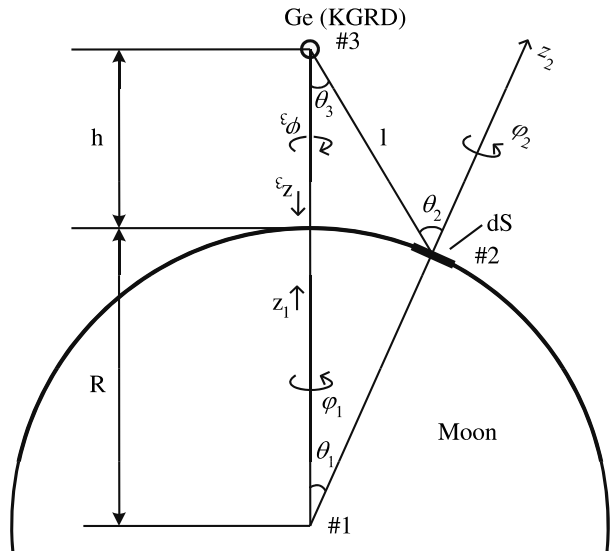
Fig. 6 The three-stage treatment of transport of gamma rays from lunar subsurface to KGRD

3.2 Overview of Gamma-Ray Transport from the Lunar Subsurface to the Ge Crystal

Some characteristic gamma rays that enter the Ge crystal give only a part of their energy to the Ge crystal because of Compton scatterings. As a result, these events contribute to the continuous gamma rays in the spectrum. The magnitude and the shape of the continuum in the measured spectrum is of importance for spectral unfolding analysis to determine the intensity of the characteristic gamma rays that come from the lunar surface (e.g., Bielefeld et al. 1976). However, the situation for the KGRS is somewhat different, because the high-energy resolution of the KGRS makes it possible to determine the gamma-ray intensity by analyzing only the peak corresponding to the original energy (photopeak) without any information about the continuum. Thus, we only use photopeaks in the KGRS's spectrum and consider the probability to detect a lunar characteristic gamma ray in a photopeak.

Here, the transport of a characteristic gamma ray from the radioactive elements (e.g. K) in the lunar subsurface to the Ge crystal is divided in three stages, as shown in Fig. 6. The first stage is the transport of a characteristic gamma ray generated in the lunar subsurface to the surface of the Moon. Many gamma rays that are generated in the subsurface cannot reach the surface, because the gamma rays are emitted isotropically from K, and half of them

go downward. In addition, some of the gamma rays emitted upward are scattered by the regolith material and lose some of their energy. Thus, the total flux (ϕ), which is in contrast to the angular flux (Φ) used later, of the characteristic gamma rays at the lunar surface is controlled by mean-free path of gamma rays for an energy loss in the lunar surface (λ) as well as the emission rate of them per a unit regolith volume ($I_v(z_2)$). In this paper, the exact definition of the total flux, ϕ, is as follows: The total flux is the number of gamma rays flowing out per unit time from a small sphere with a unit cross-sectional area, where the center of the small sphere is fixed at the border between the space and the lunar regolith. The same rigorous definition is used by Reedy et al. (1973) and the nuclear reactor theory (Bell and Glasstone 1970). The total flux in this paper is the same as the fluence rate used in the field of radiological protection (Valentine 2007).

The second stage is the transport from the lunar surface to the front of the KGRD. The probability for a gamma ray to travel to the Ge crystal is easily described by the solid angle subtended by the Ge crystal. Since the Ge crystal is surrounded by the BGO, the Plastic, the aluminum canister and various kinds of material, the transport through them is separately considered in the next stage. The second stage ends when the gamma ray arrives at the front of the KGRD. The third is the stage in which the gamma ray directed toward the Ge crystal enters the KGRD, penetrates the surrounding components of the Ge crystal, and is fully absorbed in it.

The division in the three stages, transports in the regolith, in the space and in the sensor, is very useful for planetary gamma-ray spectroscopy. For instance, one can easily obtain the gamma-ray flux at the planetary surface from the measured count rate by going up from the third stage to the second. On the other hand, the gamma-ray fluxes at the planetary surface, such as Mercury, Moon, Mars, asteroids and comets, have been strenuously studied based on the simulation for gamma-ray emission and transport in the subsurface (e.g., Reedy 1978; Brückner and Masarik 1997). The comparison of the observation data to a result of the simulation is useful for a check on the observation data and a benchmark of the simulation code. Another merit is that the separation of the second stage and the third stage simplifies the calculation of the gamma-ray transport. The enormous computational resource is required to determine the detection efficiencies of the gamma-ray sensor for any incident directions, thus it is better to extract only the gamma-ray transport in the sensor as the third stage. The second stage is described by the solid angle of the sensor and it is easily derived in many cases.

3.3 Emission and Transport of Gamma Rays in the Lunar Subsurface (Stage 1)

The abundance of chemical elements is conventionally expressed by mass concentrations in the field of lunar geochemistry. For our purpose, it is more convenient to use the number density of elements. The number density of K (N [cm^{-3}]) can be related to the mass concentration (C, [g/g]),

$$N(z_2) = \frac{N_A d}{M} C(z_2) \quad [\text{cm}^{-3}], \tag{1}$$

where, N_A is Avogadro's number, d the density of regolith in units of g/cm^3, M the atomic mass of natural K, and N is a function of depth (z_2). Natural K contains the radioactive nuclide ^{40}K, which decays with a half life (T) of 1.277×10^9 year. ^{40}K transforms to ^{40}Ar via electron capture reaction with a probability of 10.7%, and immediately emits a characteristic gamma ray with an energy of 1.461 MeV. Thus, the emission rate of the characteristic gamma rays per unit regolith volume and unit solid angle is

$$I_v(z_2) = \frac{\zeta \eta \beta}{4\pi} N(z_2) = \frac{\zeta \eta \beta N_A d}{4\pi M} C(z_2) \quad [\text{cm}^{-3} \, \text{s}^{-1} \, \text{str}^{-1}], \tag{2}$$

Fig. 7 Explanatory drawing of the transport of the gamma rays from a volume (dV) under the lunar surface to the surface (dS). In this figure, the dV is located on the z_2x_2 plane
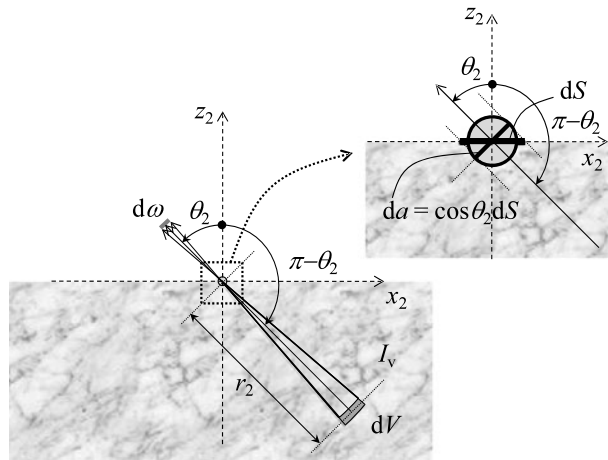
where ζ is the decay constant of ^{40}K ($\zeta = \ln 2/T$), η is the abundance ratio of ^{40}K ($\eta = 0.0117\%$), and β is the expected number of gamma rays emitted per a disintegration of ^{40}K ($\beta = 0.107$).

Here, we define the angular flux at the lunar surface, since it is useful for deriving the relationship between the emission rate in the lunar subsurface $I_v(z_2)$ and the total flux at the lunar surface ϕ. The angular flux at the lunar surface ($\Phi(\theta_2, \varphi_2)$) is defined by using the coordinate system of #2 as the number of gamma rays going out from a small sphere to the direction determined by (θ_2, φ_2) per solid angle per unit time. The small sphere has a unit cross-sectional area and the center of it is fixed at the border between the lunar surface and the space. The relationship between the total flux and the angular flux is written

$$\phi = \int d\Omega \cdot \Phi(\theta_2, \varphi_2), \tag{3}$$

where $d\Omega$ is an infinitely small solid angle and the integration is performed over the celestial hemisphere ($0 < \varphi_2 < 2\pi$, $0 < \theta_2 < \pi/2$).

Figure 7 shows how a volume in the lunar subsurface (dV) with a emission rate of $I_v(z_2)$ contributes to the number of gamma rays with the energy of 1.461 MeV crossing the cross-sectional area of a small sphere (da) or the surface parcel (dS) per a unit time. By using the angular flux and the mean free path of the gamma ray in the regolith (λ), which has a unit of cm^{-1}, the number of gamma rays flowing out from the small sphere per unit time can be expressed as

$$\left(\int d\Omega \cdot \Phi(\theta_2, \varphi_2) \right) \cdot da = \int |dV| \cdot I_v(z_2) \cdot \frac{da}{r_2^2} \cdot \exp\left(-\frac{r_2}{\lambda} \right)$$

$$= \left(\int_0^{2\pi} d\varphi_2 \int_0^{\frac{\pi}{2}} \sin\theta_2 d\theta_2 \int_0^{\infty} \exp\left(-\frac{r_2}{\lambda} \right) \right.$$

$$\left. \cdot I_v(r_2 \cos(\pi - \theta_2)) \cdot dr_2 \right) \cdot da$$

$$= \left(\int d\Omega \cdot \left[\int_0^{\infty} dr_2 \cdot \exp\left(-\frac{r_2}{\lambda} \right) \right. \right.$$

$$\left. \cdot I_v(-r_2 \cos(\theta_2)) \right] \right) \cdot da \quad [\text{s}^{-1}], \tag{4}$$

where da/r_2^2 is the solid angle subtended at the position of dV by the small sphere, and $\exp(-r_2/\lambda)$ is the attenuation rate of the gamma rays that are directed to the small sphere from dV. The integration of the left-hand side of (4) is performed over the celestial hemisphere and the right-hand side is performed over the lunar regolith, which is assumed as a semi-infinite slab. From (4), the angular flux at the lunar surface is derived;

$$\Phi(\theta_2, \varphi_2) = \int_0^\infty dr_2 \cdot \exp\left(-\frac{r_2}{\lambda}\right) \cdot I_v(-r_2 \cos \theta_2) \quad [\text{cm}^{-2}\,\text{s}^{-1}\,\text{str}^{-1}]. \tag{5}$$

In the case that the vertical distribution of K is assumed to be uniform in the lunar subsurface because of the reworking by the meteorites, I_v is constant. Then the angular flux is reduced to

$$\Phi(\theta_2, \varphi_2) = \lambda I_v \quad [\text{cm}^{-2}\,\text{s}^{-1}\,\text{str}^{-1}]. \tag{6}$$

Equation (6) means that the angular flux is isotropic, when $\theta_2 < \pi/2$. From the relation of (3), we can calculate the total flux at the surface (ϕ) in the case that the vertical distribution of K is uniform in the regolith;

$$\phi = \int_0^{2\pi} d\varphi_2 \int_0^{\frac{\pi}{2}} \Phi \sin \theta_2 d\theta_2 = 2\pi \lambda I_v \quad [\text{cm}^{-2}\,\text{s}^{-1}]. \tag{7}$$

It means that the total flux of the characteristic gamma rays at the lunar surface is proportional to the emission rate and the mean-free path.

For convenience, the number of gamma rays crossing the surface parcel per unit area per unit time (I_a) is given;

$$I_a = \int_0^{2\pi} d\varphi_2 \int_0^{\frac{\pi}{2}} (\Phi \cos \theta_2) \sin \theta_2 d\theta_2 = \pi \lambda I_v = \frac{\phi}{2} \quad [\text{cm}^{-2}\,\text{s}^{-1}], \tag{8}$$

since the angular flux is decreased by a factor of $\cos \theta_2$ as shown in the inset of Fig. 7. Equation (8) indicates that the total flux ϕ is exactly twice as large as I_a, which is also derived by Reedy et al. (1973).

3.4 Transport from the Lunar Surface to the Ge Crystal (Stage 2 and 3)

The second stage is the transport of gamma rays from the lunar surface to the front of the KGRD, as shown in Fig. 6. The probability of a gamma ray escaping from a parcel at (R, θ_1, φ_1) to deposit its full energy in the Ge crystal is proportional to the solid angle subtended by the Ge crystal (ω). The solid angle is generally a function of the incident direction and thus $\omega = \omega(\theta_1, \varphi_1)$ and can be expressed as

$$\omega \cong \frac{\sigma}{l^2}(\theta_1, \varphi_1) \quad [\text{str}], \tag{9}$$

where σ is the maximum cross-sectional area of the Ge crystal cut by the plane perpendicular to the line of sight. This is easily calculated based on the Monte Carlo method, as demonstrated in Sect. 4.2.

The gamma rays delivered within the solid angle and reaching the KGRD must penetrate some components around the Ge crystal, such as the BGO, the Plastic, and the aluminum

canister, without any scatterings to deposit its full energy in the Ge crystal (the third stage in Fig. 6). As shown in Figs. 1 and 2, the arrangement of the components is not symmetric and the photopeak efficiency is generally a function of both the incident direction and the position from which the gamma ray enters into the Ge crystal. However, the trajectories of gamma rays coming from a small parcel at (R, θ_1, φ_1) are presumed to be practically parallel to one another at the position of the KGRD, although some of the gamma rays penetrate the Ge crystal near its center and others graze it. Thus, we introduce the photopeak efficiency averaged for the gamma rays incident from the parcel at (R, θ_1, φ_1), that is

$$\epsilon = \epsilon(\theta_1, \varphi_1). \tag{10}$$

This average photopeak efficiency can also be calculated using the simulation model of the KGRD.

3.5 The SRF that Bridges Between the Count Rate at the Orbit and the Gamma-Ray Flux at the Lunar Surface

Now, it is possible to derive the count rate of 1.461 MeV by using Φ, ω and ε. The count rate of the 1.461 MeV gamma rays contributed from the parcel at (R, θ_1, φ_1) is equal to $\varepsilon\omega\Phi \cdot \cos\theta_2 dS (= \varepsilon\omega\Phi \cdot da)$. The gamma rays absorbed in the Ge crystal more or less come from any place on the lunar surface within the FOV. Thus the total count rate of 1.461 MeV (R) is given by

$$R = \iint_{FOV} \epsilon(\theta_1, \varphi_1) \cdot \omega(\theta_1, \varphi_1) \cdot \Phi(\theta_1, \varphi_1) \cdot \cos\theta_2 dS \quad [s^{-1}], \tag{11}$$

where the integration is performed over the lunar surface within the FOV. Substituting (6) and (7), (11) is transformed to

$$R = \iint_{FOV} \phi(\theta_1, \varphi_1) \cdot \Pi(\theta_1, \varphi_1) dS \quad [s^{-1}], \tag{12}$$

where, $\Pi(\theta_1, \varphi_1)$ is the SRF defined as

$$\Pi(\theta_1, \varphi_1) = \frac{1}{2\pi} \cdot \epsilon(\theta_1, \varphi_1) \cdot \omega(\theta_1, \varphi_1) \cdot \cos(\theta_2(\theta_1)). \tag{13}$$

The value of the SRF is proportional to the probability that a characteristic gamma ray emitted at (R, θ_1, φ_1) is fully absorbed in the Ge crystal. Conversely, we can interpret the SRF as the directional sensitivity of the KGRS to the lunar surface. In this context, the shape of SRF can be used to investigate the anisotropic response of the KGRS.

As seen in (12), the derivation of gamma-ray flux at the surface is involved in deconvolution problem. There are several ways to solve (12) and to obtain $\phi(\theta_1, \varphi_1)$ (e.g., Haines et al. 1978; Lawrence et al. 2007), but the method that is the easiest and the most reliable in obtaining the surface flux is shown here at the expense of spatial resolution. Assuming that ϕ is almost constant in an area centered at the nadir point, ϕ is approximated:

$$\phi(nadir) \sim R \cdot \left(\iint_{FOV} \Pi(\theta_1, \varphi_1) dS \right)^{-1} \quad [cm^{-2} \, s^{-1}]. \tag{14}$$

R can be obtained from the observational data of KGRS by analyzing the gamma-ray peak at 1.461 MeV and the integration of SRF is possible if the SRF is known. Equation (14) connects the count rates at the orbit to the total flux at the lunar surface.

3.6 Coefficient to Derive Mass Concentration of Potassium

It is very useful to derive the coefficient that converts the count rate of 1.461 MeV directly to the abundance of K in the lunar subsurface. First, we introduce the effective cross section of the KGRD (s):

$$s = \frac{1}{2\pi} \iint_{FOV} \epsilon \cdot \omega \cdot \cos\theta_2 dS \quad [\text{cm}^2], \tag{15}$$

which is the equivalent cross section of the KGRD if the KGRD is put on the lunar surface and has a 100% photopeak efficiency for 1.461 MeV. Equation (14) is simplified by using (15) as

$$R \sim s\phi \quad [\text{s}^{-1}]. \tag{16}$$

By using this effective cross section and the observed count rate, the mass concentration of K is derived from (2), (7) and (16):

$$C = \frac{4\pi M}{\zeta \eta \beta N_A d} I_v = \frac{2MR}{\zeta \eta \beta N_A \Lambda s}, \tag{17}$$

where $\Lambda(= \lambda d)$ is the mean-free path of a gamma ray with a unit of g/cm^2. The conversion coefficient of 1.461 MeV for the K abundance is defined as $2M/(\zeta \eta \beta N_A \Lambda s)$. Multiplying the count rate of 1.461 MeV gamma rays by this coefficient, we can obtain the absolute K abundance in the lunar subsurface.

4 Calculation of Individual Components

The angular flux of gamma rays at the lunar surface, the solid angle, and the average photopeak efficiency are the parameters that determine the SRF and the count rate of gamma rays, as given in (11) and (13). In this section, these parameters are calculated and their characteristics are discussed.

4.1 The Angular Flux at the Lunar Surface (Φ)

The angular flux of the characteristic gamma rays at the lunar surface is characterized by the emission rate $I_v(z_2)$ and the mean-free path of gamma ray in the regolith λ as shown by (5). Here, the condition in which the natural radioactive elements are uniformly distributed in terms of depth is assumed. Thus, the angular flux in this condition is expressed in (6).

It is important to remember that in the lunar gamma-ray remote sensing, the mean-free path of gamma rays in the lunar regolith is not so strongly affected by the variation of composition of lunar surface regolith (Prettyman et al. 2006). The mean-free paths in units of g cm^{-2}, Λ, in the regoliths with the composition of Apollo 11 and 16 sites (Heiken et al. 1991) were calculated by using XCOM (Berger et al. 2005) and shown in Fig. 8. Iron and titanium, which have high atomic numbers (Z), are more abundant in Apollo 11 soil than in Apollo 16 soil (A11 and A16, respectively). As a result, characteristic gamma rays are more absorbed in A11 than A16 because the probability of photoelectric absorption is proportional to Z^5. The mean-free path in A11 at low-energy range (< 0.2 MeV), where photoelectric effects dominate, becomes lower than that in A16. In the same way, the mean-free path in A11 is more decreased by the absorption due to the pair production process in comparison with A16. The probability of this is proportional to Z^2 and the absorption by

Fig. 8 Mean-free path of gamma rays in lunar soil at Apollo 11 (A11) and 16 sites (A16). Ratio of the two is also shown (A11/A16)
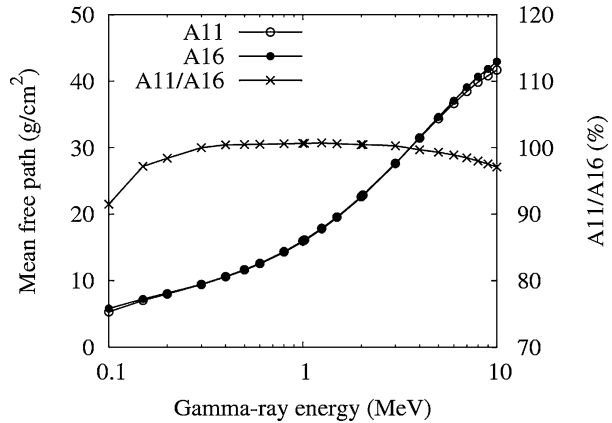
Fig. 9 Solid angle subtended by the Ge crystal of KGRD viewed from the lunar surface point (X, Y). The unit of the color bar is steradian. The resolution of this image is about 20 km within 200 km from the origin
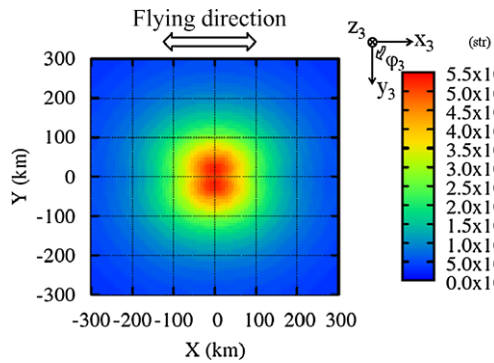
the pair production occurs more frequently in A11 than A16 at high energies ($\gtrsim 8$ MeV). However, the difference of Λ between A11 and A16 is within 2% in the energy range from 0.2 to 8 MeV where most of the characteristic gamma rays that are used to investigate the lunar materials are detected. For the calculations in this paper, the mean-free path of gamma rays in A16 is alternatively used since the variation of mean-free path over the lunar surface is sufficiently constant.

4.2 Solid angle (ω)

The solid angle subtended by the Ge crystal was derived according to (9). First, the projected areas of the Ge crystal σ, viewed from various directions, were calculated using the Monte Carlo method. Second, each σ was divided by the square of the distance l from a point on the lunar surface to the KGRD. Eventually, the solid angles viewed from 6841 directions on the lunar surface in the FOV were calculated. The contour plot of the solid angle subtended by the Ge crystal viewed from a lunar surface point $(X, Y) = (R \sin\theta_1 \cos\varphi_1, R \sin\theta_1 \sin\varphi_1)$ is shown in Fig. 9. The nadir of the KGRD is located at the origin of the graph. The Kaguya spacecraft moved in the direction of $+x_3$ or $-x_3$, which was switched by the yaw-around operation every 6 months to adjust the orientation of the Kaguya's solar paddle. The solid angle decreases with the distance l from the overall viewpoint, but the contour plot is slightly affected by the cylindrical shape of the Ge crystal. Because the Ge crystal is installed with its

Fig. 10 The average photopeak efficiency of the level 2 KGRD model for a gamma ray incident from the lunar surface point (X, Y) with energy of 1.5 MeV. The unit of color bar is %. The resolution of this image is about 20 km within 200 km from the origin
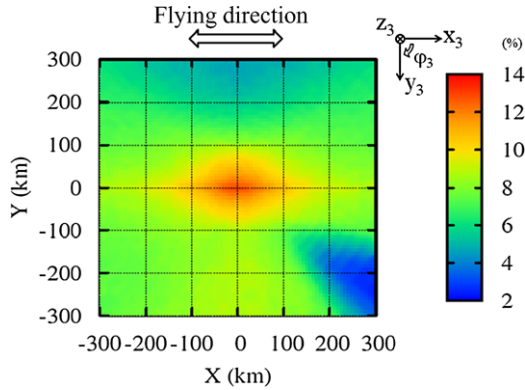
4.3 Average Photopeak Efficiency (ε)

The average photopeak efficiencies were calculated using Geant4.8.3 with the simulation model discussed in Sect. 2.2. A monochromatic gamma-ray beam, the diameter ($2b$) of which completely included the Ge crystal, was irradiated from the outside of the KGRD, and the average photopeak efficiencies for the 6841 incident directions were calculated for energies from 0.2 to 10 MeV. The number of gamma rays generated in the simulation (N_{beam}) was 50000 for one direction, and we counted the number of events in which the energy was fully deposited in the Ge crystal (N_{abs}). The average detection efficiency is determined by the equation, $\varepsilon = \pi b^2 N_{\text{abs}} / (\sigma N_{\text{beam}})$.

The average photopeak efficiency for the level 2 model is shown in Fig. 10 for the case of 1.5 MeV. It is obvious from Fig. 10 that the surrounding components affect the photopeak efficiency. The efficiency is slightly low in the direction of $\varphi_3 = 270°$ and considerably lower for $\varphi_3 = 45°$ because the incident gamma rays are interrupted by the thick BGO crystal and the compressor, respectively. Contrary to above, the efficiency becomes higher in the direction of $\varphi_3 = 0°, 90°$ and $180°$ because the BGO is relatively thinner for these directions.

5 Characteristics of the SRF of the KGRS

### 5.1 The Spatial Response Function

The KGRS's SRF was calculated according to (13) for the sphere, the level 1, and the level 2 model. Since the average photopeak efficiency is a function of gamma-ray energy, the SRF also depends on it. Refer to Hasebe et al. (2008) for the SRF using the level 1 model. Here, the SRF calculated by the level 2 model is discussed. For example, the KGRS's SRF for 1.5 MeV normalized by the value at the nadir is shown in Fig. 11. The anisotropic response of the average photopeak efficiency in Fig. 10 is considerably reduced, and the response of the KGRS is almost isotropic at 1.5 MeV. The strong dependence of ε on the arrangement of surrounding components of the Ge crystal is attenuated by multiplying the solid angle and the factor of $\cos\theta_2$, both of which decrease with distance from the nadir.

The cross sections of the SRF for 1.5 MeV and 0.2 MeV at an altitude of 100 km are shown in Figs. 12 and 13, respectively. The LPGRS' SRF at 100 km altitude and 0° latitude

Fig. 11 The normalized SRF of KGRD for 1.5 MeV at the altitude of 100 km. The unit of color bar is %. See Fig. 14 for the FWHM of this SRF. The resolution of this image is about 20 km within 200 km from the origin
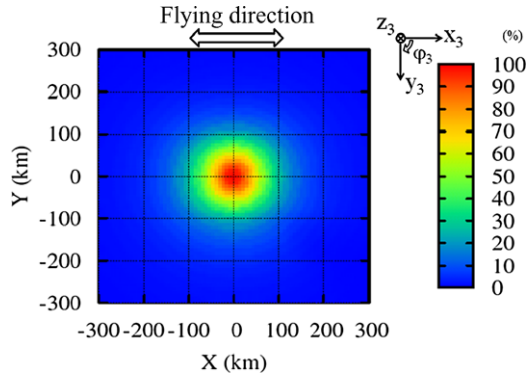
Fig. 12 The cross sections of the normalized SRF for 1.5 MeV at the altitude of 100 km. See Fig. 14 for the FWHM of this SRF. The SRF of LPGRS at 100 km and at 0° latitude used for the analysis of 2.6 MeV from Th by Lawrence et al. (2003) is also shown
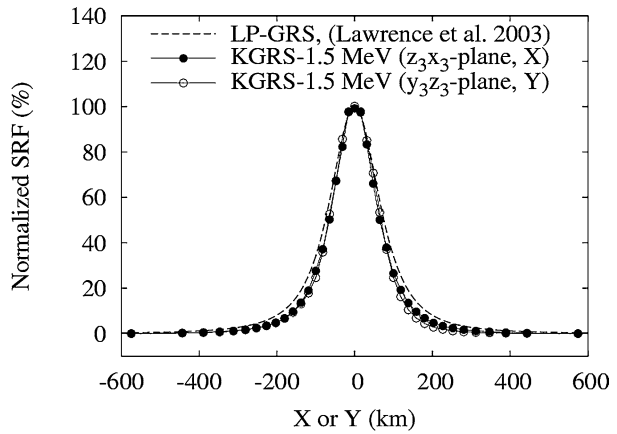
Fig. 13 The cross sections of normalized SRF for 0.2 MeV at the altitude of 100 km. See Fig. 14 for the FWHM of this SRF. The SRF of LPGRS at 100 km and at 0° latitude used for the analysis of 2.6 MeV from Th by Lawrence et al. (2003) is also shown
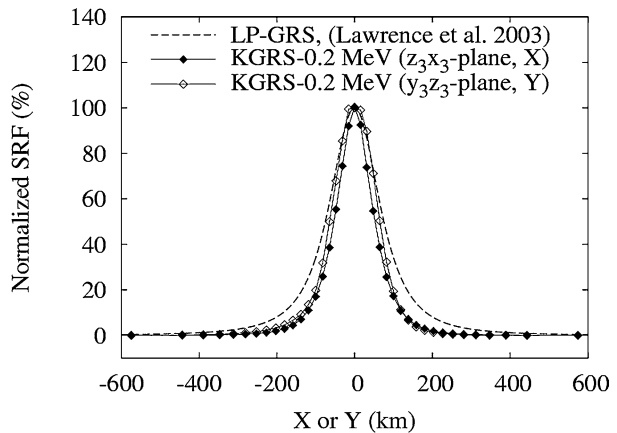
is also shown, which is used for the analysis of 2.6 MeV of Th in the paper by Lawrence et al. (2003). The LPGRS's SRF is a function of the lunar latitude since Lunar Prospector was a spin-stabilized satellite, and the incident direction of lunar gamma rays changed according to the lunar latitude. Alternatively, the KGRS's SRF is independent of latitude because the

attitude of KGRS relative to the lunar surface was kept independently on the latitude by the reaction wheels of Kaguya. As seen in Fig. 12, the shape of the SRF for 1.5 MeV projected on z_3x_3-plane is very similar to that on y_3z_3-plane. Their shapes are also similar to that of LPGRS, but are slightly narrower. On the other hand, the SRF for 0.2 MeV gamma rays, which is the nominal lower limit of the energy spectrum of the KGRS, has moderate anisotropy. In addition, the SRF is sharper than that of 1.5 MeV, which indicates that the spatial resolution for 0.2 MeV is high in comparison with that for 1.5 MeV. This is due to the horseshoe shape of the BGO (see Fig. 1b). As seen in Fig. 1b, some of the gamma rays originated from the lunar surface must go through the BGO with a thickness of 1–3 cm, so as to be absorbed in the Ge crystal. The shielding by the BGO against incident gamma rays from the lunar surface works more effectively for lower energy, and the SRF at 0.2 MeV becomes sharpened in comparison with that at 1.5 MeV.

5.2 Spatial Resolution

There are some definitions of spatial resolution in the field of gamma-ray remote sensing: One definition is the full width at half maximum of the SRF (e.g., Lawrence et al. 2003), and another is the radius (or diameter) of the footprint from which 50% of the total count rate of gamma rays are received (e.g., Boynton et al. 2004). The former definition is used in this paper, but note that the FWHM depends on the plane on which the KGRS's SRF is projected.

The spatial resolution of the KGRS at an altitude of 100 km was calculated using the level 2 model and is shown in Fig. 14. The spatial resolution of the KGRS is dependent on the energy of incident gamma rays and the plane on which the SRF is projected. It ranges from 100 to 140 km and is about 130 km for 1.5 MeV. The spatial resolution of the KGRS based on the level 2 model is a little smaller than that of the sphere model ($= 147$ km). This result is easily understood because the Ge crystal is almost completely surrounded by the heavy and thick BGO crystal, which effectively limits the scope of the KGRD. The FWHM of the SRF is fairly constant above 0.8 MeV, and the difference between the FWHM on y_3z_3-plane cross section and that of z_3x_3-plane is less than 5%. With decreasing the gamma-ray energy from 1.5 MeV, the SRF is compressed from the directions of $\varphi_3 = 0°$, $180°$ and becomes oval-shaped. The FWHM of the SRF projected on the z_3x_3-plane (FWHM-z_3x_3) has considerable energy dependence because gamma rays with low energy are readily absorbed or scattered by the horseshoe-shaped BGO (see Fig. 1b). This shielding effect works very effectively because both sides of the Ge crystal are protected by the BGO (Fig. 1b). On the other hand, the change of the FWHM-y_3z_3 with energy is moderate. The shielding

Fig. 14 The spatial resolution of the KGRD (FWHM) at the altitude of 100 km. The *dashed line* shows the spatial resolution for the case of sphere model (147 km)
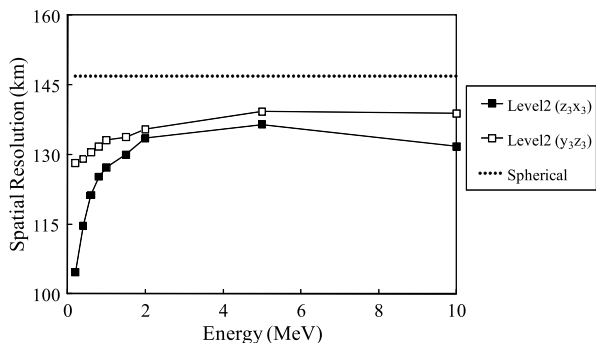
Fig. 15 The effective cross sections of KGRD for the sphere, level 1 and level 2 models
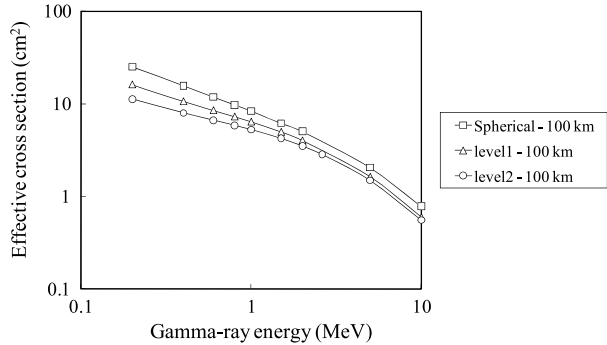
effect of surrounding components becomes relatively low because the thickness of the material for the radiator side is thin and only the PMT side is covered with BGO. The ratio of FWHM-z_3x_3 to FWHM-y_3z_3 is more than 90% above 0.5 MeV and 82% above 0.2 MeV.

5.3 Conversion Coefficients

The integration of the SRF over the whole lunar surface in the FOV gives the effective cross section (s) of the KGRD that converts the count rates to the flux of gamma-ray lines on the lunar surface ((15) and (16)). The effective cross section as a function of gamma-ray energy is shown in Fig. 15. To evaluate the influence of surrounding materials, the cross sections calculated by using the simple models, the sphere and the level 1, are also shown. The more sophisticated the KGRD model is, the smaller the cross sections become. This means that the BGO crystals and the aluminum canister around the Ge crystal shield incident gamma rays and reduce its sensitivity, although they are indispensable as the constituents of the KGRD. The effective cross section of the KGRD is 11 cm^2 for 0.2 MeV, and it is about 4.3 cm^2 for 1.461 MeV from ^{40}K. The cross section for 10 MeV becomes nearly one-tenth as large as that of 1 MeV. An example of this cross section usage is given: If the surface flux of 1.461 MeV gamma rays is 1 cm^{-2} s^{-1}, the count rate of 1.461 MeV peak recorded by the KGRD is 4.3 s^{-1}.

In the case of natural radioactive elements, the conversion of count rate of a gamma-ray peak to the absolute abundance is discussed in Sect. 3. Examples of the conversion coefficient and the constants that are necessary to calculate it are shown in Table 1a and b for 1.461 MeV from ^{40}K and 0.911 MeV from ^{228}Ac that is a daughter nuclide of ^{232}Th. The way to derive these conversion coefficients differs from one nuclide to another because the mode of production and decay of the nuclide that emits a characteristic gamma ray is unique to the nuclide. But the coefficients and the physics necessary to derive the conversion coefficient are well known, and it is easily obtained.

The conversion coefficients for some major and minor peaks from the natural radioactive elements are summarized in Table 2. These are calculated by using the level 2 model of the KGRD. The accuracy of these coefficients could be determined by the simulation model of level 2 and the systematic error is estimated to be less than 8%.

Because of the great energy resolution of the KGRS, three photopeaks (0.239, 0.911 and 2.615 MeV) are easily available for the analysis of Th abundance, although 0.239 MeV peak is interfered by two adjacent peaks of 0.241 and 0.242 MeV from Th and U, respectively. If the spectrum is analyzed in detail, additional peaks (e.g., 0.727 and 0.969 MeV) would be available for Th abundance. Likewise, 3 peaks (0.352, 0.609 and 1.764 MeV) are immediately useful for the determination of U abundance. However, only one peak of 1.461 MeV

Table 1 (a) The parameters for the conversion coefficient for the 1.461 MeV from K. (b) The parameters for the conversion coefficient for the 0.911 MeV from Th

(a)

M	Average molecular mass	39.10	g/mol
s	Effective cross section of KGRD	4.32	cm^2
Λ	Mean free path of the gamma ray	19.2	g/cm^2
ζ	Decay constant of ^{40}K	1.72×10^{-17}	s^{-1}
$\beta = P_p P_g$	Probability for ^{40}K to emit 1.461 MeV after the decay	10.7%	
P_g	Probability for ^{40}Ar to emit 1.461 MeV	100%	
P_p	Probability of production of ^{40}Ar	10.7%	
η	Natural abundance of ^{40}K	0.0117%	
N_A	Avogadro constant	6.02×10^{23}	mol^{-1}
	Conversion coefficient	7284	ppm/cps

(b)

M	Average molecular mass	232	g/mol
s	Effective cross section of KGRD	5.53	cm^2
Λ	Mean free path of the gamma ray	15.2	g/cm^2
ζ	Decay constant of ^{232}Th	1.56×10^{-18}	s^{-1}
$\beta = P_p P_g$	Probability for ^{228}Ac to emit 0.911 MeV after the decay	26%	
P_g	Probability for ^{228}Th to emit 0.911 MeV	26%	
P_p	Probability of production of ^{228}Th	100%	
η	Natural abundance of ^{232}Th	100%	
N_A	Avogadro constant	6.02×10^{23}	mol^{-1}
	Conversion coefficient	22.79	ppm/cps

Table 2 Conversion coefficients for the major peaks of natural radioactive elements

Elements	Nuclide	Energy (MeV)	Conversion coefficient (ppm/cps)
K	^{40}K	1.461	7284
Th	^{212}Pb	0.239	12.39
Th	^{224}Ra	0.241	130.9
Th	^{228}Ac	0.911	22.79
Th	^{208}Tl	2.615	18.96
U	^{214}Pb	0.242	23.74
U	^{214}Pb	0.352	4.895
U	^{214}Bi	0.609	4.199
U	^{214}Bi	1.764	12.98

is available for K abundance. In the case that multiple peaks are available to determine the abundance of a radioactive element, the abundances derived from each peak should ideally agree with one another. If the agreement fails because of the presence of a hidden peak, the uncertainty of continuum background, and the contribution of background gamma rays from surrounding materials, we can realize the misanalysis of gamma-ray peaks. This self-examination is an advantage of the KGRS in comparison with the previous lunar gamma-ray
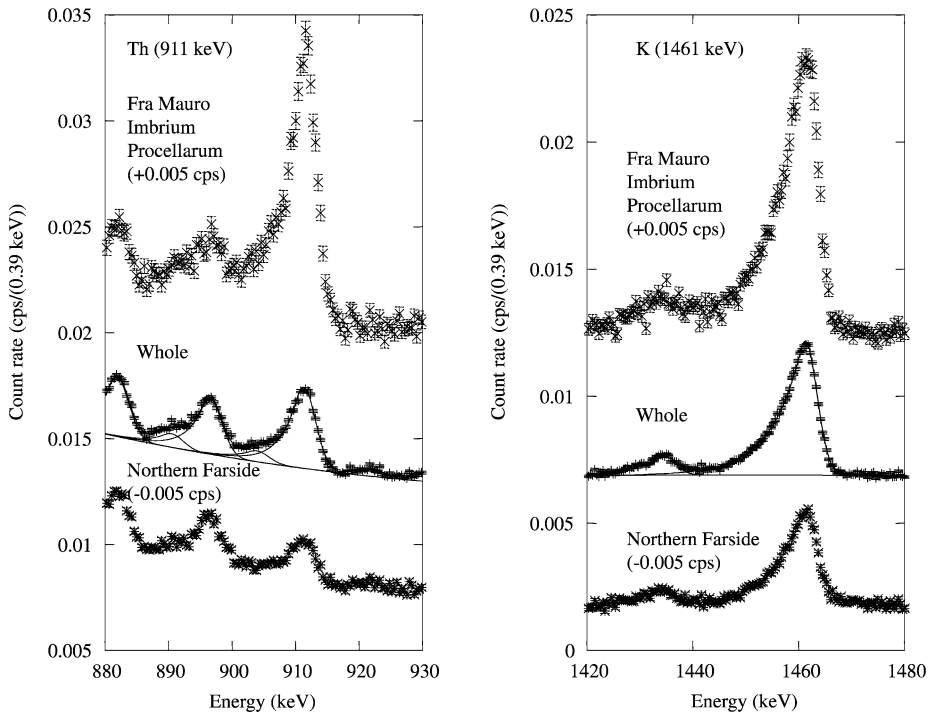
Fig. 16 The energy spectra of Th and K of 911 keV and 1461 keV, respectively. The spectra at top are integrated in the nearside region (lat. 0°–60°, lon. −60°–0°), which corresponds to Fra Mauro, Imbrium and Procellarum. Spectra at bottom are accumulated in the northern farside (lat. 0°–90°, lon. 90°–180° and −180°–(−90°)). The spectra indicated as "Whole" are summed during the whole of Period 1, which is December 14, 2007, to February 17, 2008. For ease of identification, the top and the bottom spectra are moved by +0.005 cps and −0.005 cps, respectively

remote sensing missions and is easily made using the conversion coefficients tabulated in Table 2.

6 The Absolute Abundances of K and Th Derived by the Current Method

To check the ability of method discussed here for the determination of the absolute abundances, preliminary data analysis was made using KGRS data obtained from December 14, 2007, to February 17, 2008. In this period and in the nominal mission, the Kaguya flew at an average altitude of 100 km, while the altitude was lowered to 50 km in the extended mission. Here, K and Th abundances are derived by analyzing the characteristic gamma rays of 1.461 MeV from ^{40}K and 0.911 MeV from ^{228}Ac, respectively (see Fig. 16). Both K and Th are known to be considerably concentrated in the lunar nearside, especially the regions of Fra Mauro, Imbrium and Procellarum, whereas there are little K and Th in the northern farside (Lawrence et al. 1998, 2000). These peaks and variations of their count rate were clearly identified by the KGRS spectra, as shown in Fig. 16.

First, the lunar surface was pixelated by 450 × 450 km quasi-equal areas, gamma-ray counts were accumulated in each pixel, and 190 spectra were made. Corrections to count rate variations due to variations in the altitude of Kaguya spacecraft were not yet performed,

but the systematic error due to it was less than $\pm 4\%$. The count rates of photopeaks at 0.911 MeV from Th and 1.461 MeV from K in 190 spectra were analyzed on the basis of the total peak area method (Gilmore and Hemingway 1995), which derived the peak areas with the linear approximation of background continuum. Since the total peak area method tends to indicate a smaller value than the true one, the count rates were modified by factors (δ) that correct the difference between the peak analysis by the total peak area method and that by the peak fitting method. These factors were derived by comparing the results between the two methods for the globally integrated spectrum, and were $\delta_{1.461} = 1.12 \pm 0.07$ and $\delta_{0.911} = 1.16 \pm 0.08$ for 1.461 MeV and 0.911 MeV, respectively. Finally, the modified count rates were converted to the absolute abundances using the conversion coefficients in Table 2.

There are background gamma rays from K and Th included in the materials around the Ge crystal and/or those from the spacecraft material that emits almost the same energies as 0.911 and 1.461 MeV by the excitation due to the interactions of cosmic rays. Thus, we have made the measurements of background gamma rays by shielding the lunar gamma rays with the spacecraft body and the BGO. Throughout the background measurement operation, the attitude of the Kaguya spacecraft was controlled to be fixed in the inertial coordinate system, while the three-axis control mode that oriented $+z_3$-axis to the center of the Moon was applied during the normal operation. Hence $+z_3$-axis was directed toward the deep space and the lunar gamma rays were shielded by the spacecraft body and the BGO during about 25% of one revolution of the spacecraft around the Moon, assuming that the scope of the KGRD is defined as $\pm 45°$ (the aperture angle of the BGO is $\pm 45°$; see Fig. 1b). The background measurement operations were performed in July and Dec. 2008 and the Kaguya spacecraft was in this mode for 21 revolutions in total. Moderate background was found at 1.461 MeV with 95% confidence limit (c.l.) during the background measurement. It was preliminarily estimated as 115 µg/g ($=$ ppm) of K in the lunar surface abundance equivalent and was subtracted from the absolute abundance obtained above. For 0.911 MeV, the statistically valid background was not detected in this preliminary analysis with 95% c.l., and we have made no subtraction here. The detailed analysis of the backgrounds will be needed and will be published elsewhere in the future.

Figure 17 shows the global map of K abundance created using The Generic Mapping Tools (GMT, Wessel and Smith 1991). The K abundances in quasi-equal area pixels processed above were smoothed by the natural bicubic spline interpolation to make the map and the shaded relief was created from the topography data obtained by the Kaguya laser altimeter (Araki et al. 2009). The random errors of K abundances in each pixel range from 119 to 230 ppm, thus the K abundances in the lunar farside should be used with care. The enhancement of K in Aristarchus region observed by the LPGRS (Prettyman et al. 2006) is obscured in Fig. 17. One of the reasons could be due to the accumulation of spectra over the relatively large area (450×450 km^2).

The correlation plot between K and Th abundances on the lunar surface determined by the current method is shown in Fig. 18. The random errors of Th abundances that are shown in Fig. 18 are between 0.13 and 0.66 ppm. The regression line in Fig. 18 was determined by York's method (York 1966, 1969), taking into accounts both the errors of K and Th abundances. The slope of the line is 346 ± 11 (random) $+60/-52$ (systematic). The random error of the slope consists of the counting statistics of gamma rays and the errors of $\delta_{0.911}$ and $\delta_{1.461}$, while the systematic error is estimated by the 8% ambiguity of the level 2 model. The result of the KGRS is comparable to the data of lunar materials (K/Th $= 397$, Korotev 1998), early LPGRS results calibrated by lunar materials (K/Th $= 318$, Gillis et al. 2004) and the latest results of LPGRS (K/Th $= 359$–368, Prettyman et al. 2006). This consistency is real because K and Th abundances were determined absolutely and independently of each
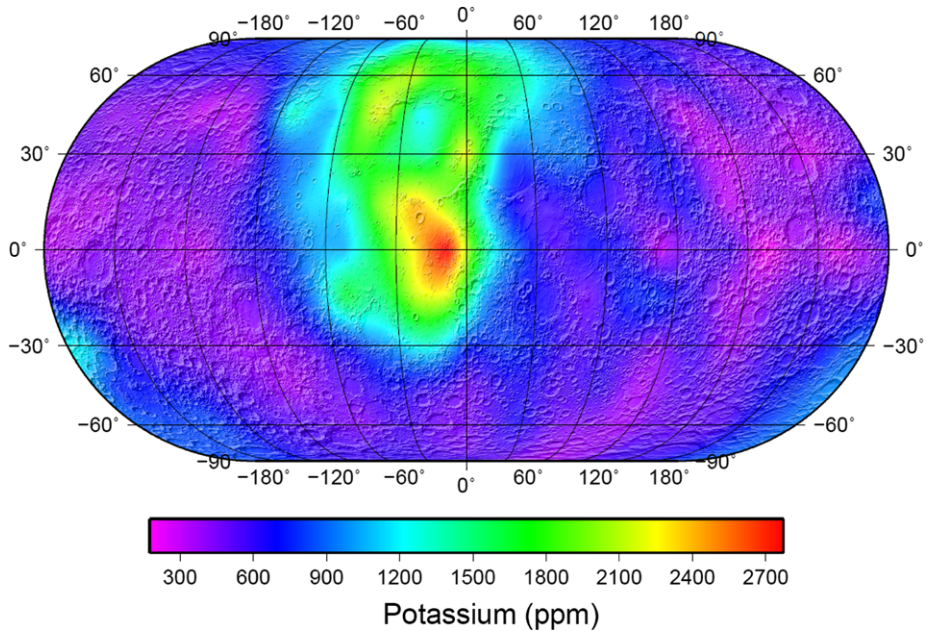
Fig. 17 Global map of K that was made by smoothing data points, 450 km × 450 km quasi-equal area pixels, by a natural bicubic spline interpolation. Note that the errors of K abundances are 119 to 230 ppm. The shaded relief was created from the topographic data by the Kaguya laser altimeter

Fig. 18 Correlation of the K and Th abundances averaged in 450 × 450 km quasi-equal area pixel measured by KGRS
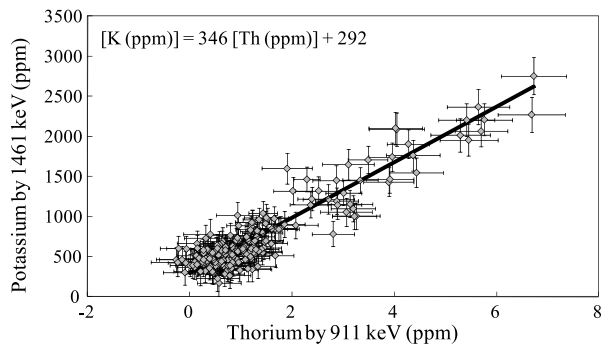
other without any information on ground truths, lunar meteorite analyses and past remote sensing data. It is obvious that KGRS data analyzed by the current method is powerful in determining the absolute abundances of K and Th on the lunar surface.

The maximum K and Th abundances occur near Fra Mauro region (lat. $-7.4°$ to $+7.4°$, lon. $-15°$ to $0°$), and are 2753 ± 153 (random) ± 248 (systematic) ppm and 6.7 ± 0.5 (random) ± 0.6 (systematic) ppm, respectively (These are the average concentrations in the area of 450×450 km^2). The random errors are attributed to the counting statistics, and the error of the δ factors; the systematic errors come from the ambiguity of level 2 model (8%) and the uncorrection for the variation in the altitude of the Kaguya spacecraft in this pixel (1%). The amounts of K and Th in this analysis are smaller than the values reported by the LPGRS. Prettyman et al. (2006), who reported the latest results of LPGRS observation, presented K

maps based on 60×60 km^2, 150×150 km^2, and 600×600 km^2 pixels and the maxima of the range of K abundances were 4400, 3770 and 3300 ppm, respectively. They also showed Th maps with the same pixel sizes above, and the maxima were 11.8, 11.0 and 9.3 ppm, respectively. The spatial resolution of the LPGRS, i.e., the FWHM of its SRF, is almost the same as that of the KGRS (see Fig. 12). Thus their maps are comparable to the map presented here although the sizes of pixels are different from our current analysis. By linear regression between the abundances and the side lengths of the pixels of the LPGRS's maps, the LPGRS gives 3500 ppm K and 10 ppm Th in 450×450 km^2 pixel equivalent. Comparing the maxima by the KGRS with those by Prettyman et al. (2006), the abundances measured by the KGRS are lower about 20–30% than those by the LPGRS and are out of the margins of errors. It means that the KGRS gives lower concentrations of K and Th for Fra Mauro region than the LPGRS. The reason for the difference is unknown at present.

In the northern farside, K abundances are mostly less than 650 ppm for 450×450 km^2 (see Fig. 17) and Th abundances are typically less than 1 ppm. The absolute abundances and their distributions of K and Th in the lunar farside highland are of importance for checking the Haskin model about the distribution of Imbrium ejecta (Haskin 1998), for deducing the source region of the lunar meteorite with extremely low Th containing clasts of magnesian anorthosites that is believed as a representative of the early lunar crust (Takeda et al. 2006), and for the estimation of the bulk abundance of refractory elements of the Moon (Jolliff et al. 2000; Warren 2005). However, the measurement errors of the abundances become relatively large in the lunar farside because of the low gamma-ray fluxes of K and Th. Thus further studies are necessary to improve the accuracy of the abundances in the farside highland. The lists of studies to improve the accuracy of the abundances of K and Th in the farside highland are shown at the end of this section. We intend to determine the absolute abundances of K, Th and U precisely in the lunar farside in the future.

1. *The Reduction of the Errors During the Peak Analysis.*

    The major ambiguity of the abundances of K and Th in the lunar farside is attributed to the statistics of gamma-ray counting. The peak analyses of K and Th are based on the total peak area method in which the error of the net count rate is subject to the Poisson statistics of gamma-ray counting and the ambiguity of the gamma-ray continuum below the target peak (baseline). Both the former error and the latter will be improved by using the whole data set obtained by KGRS during the mission. Only about 20% of the total data was processed in this study. The latter can also be improved by optimizing the way to determine the baseline (Gilmore and Hemingway 1995). The error of the factor δ needs to be improved.

2. *The Studies of Background Gamma Rays at the Target Peak or Around It.*

    The material used in the KGRD and the spacecraft body contain K, Th and U in some degrees, and they could become sources of background for the measurement of lunar K, Th and U. The measurements of gamma rays from the local materials were performed as described above, and the preliminary estimates of the background derived on the basis of Gilmore and Hemingway (1995), are used in the current analysis. However, the more careful analysis of the background data and the evaluation of the obtained results from various aspects are necessary for the confident estimation of the background fluxes.

    It is known that there are some interference gamma rays to the peaks of K, Th and U. Further studies that estimate the contribution of interference peaks to the main analytical peak are necessary in order to increase the accuracy of K, Th and U abundances in the lunar farside highland. For instance, the 352 keV gamma ray from ^{214}Pb in U decay chain is interfered by the 352 keV gamma ray from the ^{56}Fe$(n, \gamma)^{57}$Fe. Although this contribution of the Fe gamma ray to the U peak may be large, it can be estimated quantitatively by

measuring the count rate of 7632 and 7646 keV gamma rays that are emitted by the same neutron capture reaction. After the subtraction of the contribution of Fe, the obtained U abundance can be evaluated by comparing the results of the other U peaks of 609 keV and 1764 keV. The excellent energy resolution of KGRS helps to determine the interference of known and/or unknown peaks with a low flux and to estimate the contribution of the interference peak quantitatively.

3. *The Altitude Correction.*

    The correction for the variation of the altitude of the Kaguya spacecraft was not performed in this study because it is relatively small in comparison with the other errors. The error due to it is less than $\pm 4\%$ and will be corrected.

4. *The Improvement of the SRF Based on Level 2 Model.*

    The analysis of the preflight data has not been completed yet. The systematic error, the difference of the detection efficiencies calculated by using the level 2 model from those obtained by the preflight experiments, will be reduced by analyzing the rest of the pre-flight data and improving the level 2 model of the KGRD. The systematic error due to the adoption of the level 2 model is estimated to be $< \pm 8\%$ at present. The evaluation of KGRS's SRF is also empirically possible by analyzing both high- and low-altitude data on the basis of the method developed by Lawrence et al. (2003).

7 Summary

The method for deriving the abundances of natural radioactive elements of K, Th and U for the KGRS observation is developed. To bring out the best performance of the KGRS, which has the greatest spectroscopic qualities among the previous lunar gamma-ray spectrometers, we developed a three-dimensional model of KGRD for the calculation of its SRF and effective cross sections using the Monte Carlo simulation library, Geant4. The series of calculations for the determination of the SRF reveal specifically how the surrounding components of the Ge crystal affect the observation of the lunar gamma rays by the KGRS. They also yield information about the anisotropic response of the KGRS, and make the quantitative estimation for the anisotropic response possible.

The coefficients that directly convert the count rate of gamma-ray peaks to the absolute abundance were obtained for several characteristic gamma rays from K, Th and U using the SRF. The preliminary analysis of the KGRS data was accomplished, and we succeeded in determining the abundances of K and Th on the lunar surface. The correlation plot of K and Th was made by using the KGRS data, and the slope of the regression line is very consistent with the results acquired by the analysis of lunar materials and the LPGRS data. In this preliminary analysis, the Th and K abundances in the Fra Mauro region obtained by the KGRS are 20 to 30% smaller than those of the LPGRS, but the reason is unknown at present. Further analyses are necessary to determine the absolute abundances K and Th in the lunar farside highland in order to reduce the errors.

The KGRS has the ability to obtain the absolute abundances of K, Th and U on the lunar surface by itself. The KGRS also potentially has means for self-checking the obtained abundance by comparing the abundances derived by multiple peaks originated from an element (Th and U). The abundances derived by the presented method are completely independent of the analyses of the returned samples of the Moon and the lunar meteorites and the observations by past lunar gamma-ray missions, such as the AGRS and the LPGRS. Therefore, the KGRS will provide an entirely-new data set of the absolute abundances of K, Th and U on the Moon in the future.

References

S. Agostinelli et al., GEANT4—a simulation toolkit. Nucl. Instrum. Methods. A **506**, 250 (2003)

H. Araki et al., Lunar global shape and polar topography derived from Kaguya-LALT laser altimetry. Science **323**, 897 (2009)

G.I. Bell, S. Glasstone, *Nuclear Reactor Theory* (Van Nostrand Reinhold, New York, 1970)

M.J. Berger, J.H. Hubbell, S.M. Seltzer, J. Chang, J.S. Coursey, R. Sukumar, D.S. Zucker, XCOM: Photon Cross Sections Database (2005). http://www.nist.gov/physlab/data/xcom/index.cfm

M.J. Bielefeld, R.C. Reedy, A.E. Metzger, J.I. Trombka, J.R. Arnold, Surface chemistry of selected regions, in *Proc. Lunar Sci. Conf. 7th*, 2661 (1976)

W.V. Boynton et al., The Mars Odyssey gamma-ray spectrometer instrument suite. Space Sci. Rev. **100**, 37 (2004)

J. Brückner, J. Masarik, Planetary gamma-ray spectroscopy of the surface of Mercury. Planet. Space Sci. **45**, 39 (1997)

W.C. Feldman et al., Gamma-ray, neutron, and alpha-particle spectrometers for the Lunar Prospector mission. J. Geophys. Res. **109**, E07S06 (2004). doi:10.1029/2003JE002207

J.J. Gillis, B.L. Jolliff, R.L. Korotev, Lunar surface geochemistry: Global concentrations of Th, K, and FeO as derived from lunar prospector and Clementine data. Geochim. Cosmochim. Acta **68**, 3791 (2004)

G. Gilmore, J.D. Hemingway, *Practical Gamma-Ray Spectrometry* (Wiley, Chichester, 1995)

J.O. Goldsten, The NEAR X-ray/gamma-ray spectrometer. Johns Hopkins APL Tech. Dig. **19**, 126 (1998)

J.O. Goldsten et al., The MESSENGER gamma-ray and neutron spectrometer. Space Sci. Rev. **131**, 339 (2007)

E.L. Haines, M.I. Etchegaray-Ramirez, A.E. Metzger, Thorium concentrations in the lunar surface. II: Deconvolution modeling and its application to the regions of Aristarchus and Mare Smythii, in *Proc. Lunar Planet. Sci. Conf. 9th* (1978), p. 2985

N. Hasebe et al., Gamma-ray spectrometer (GRS) for lunar polar orbiter SELENE. Earth Planets Space **60**, 299 (2008)

N. Hasebe et al., First results of high performance Ge gamma-ray spectrometer onboard lunar orbiter SELENE (KAGUYA). J. Phys. Soc. Jpn., Suppl. A **78**, 18 (2009)

J. Hagerty et al., Thorium abundances on the Aristarchus plateau: Insights into the composition of the Aristarchus pyroclastic glass deposits. J. Geophys. Res. **114**, E04002 (2009). doi:10.1029/2008JE003262

L.A. Haskin, The Imbrium impact event and the thorium distribution at the lunar highlands surface. J. Geophys. Res. **103**, 1679 (1998)

G.H. Heiken, D.T. Vaniman, B.M. French, *Lunar Source Book* (Cambridge University Press, Houston, 1991), p. 346

B.L. Jolliff et al., Major lunar crustal terrain: Surface expressions and crust-mantle origins. J. Geophys. Res. **105**, 4197 (2000)

M.-N. Kobayashi et al., Germanium detector with Stirling cryocooler for lunar gamma-ray spectroscopy. Nucl. Instrum. Methods A **548**, 401 (2005)

R.L. Korotev, Concentrations of radioactive elements in lunar materials. J. Geophys. Res. **103**, 1691 (1998)

D.J. Lawrence et al., Global elemental maps of the Moon: The Lunar Prospector gamma-ray spectrometer. Science **281**, 1484 (1998)

D.J. Lawrence et al., Thorium abundances on the lunar surface. J. Geophys. Res. **105**, 20307 (2000)

D.J. Lawrence et al., Small-area thorium features on the lunar surface. J. Geophys. Res. **108**, 5102 (2003). doi:1010.1029/2003JE002050

D.J. Lawrence et al., Global spatial deconvolution of Lunar Prospector Th abundances. Geophys. Res. Lett. **34**, L03201 (2007). doi:10.1029/2006GL028530

A.E. Metzger et al., Lunar surface radioactivity: Preliminary results of the Apollo 15 and Apollo 16 gamma-ray spectrometer experiments. Science **179**, 800 (1973)

C.E. Moss, J.R. Streetman, Comparison of calculated and measured response functions for germanium detectors. Nucl. Instrum. Methods A **299**, 98 (1990)

I.G. Mitrofanov et al., The Mercury Gamma and Neutron Spectrometer (MGNS) on board the Planetary Orbiter of the BepiColombo mission. Planet. Space Sci. **58**, 116 (2010)

T.H. Prettyman et al., Gamma-ray and neutron spectrometer for the Dawn mission to 1 Ceres and 4 Vesta. Nucl. Sci. IEEE Trans. **50**, 1190 (2003)

T.H. Prettyman et al., Elemental composition of the lunar surface: Analysis of gamma ray spectroscopy data from Lunar Prospector. J. Geophys. Res. **111**, E12007 (2006). doi:10.1029/2005JE002656

R.C. Reedy, J.R. Arnold, J.I. Trombka, Expected γ ray emission spectra from the lunar surface as a function of chemical composition. J. Geophys. Res. **78**, 5847 (1973)

R.C. Reedy, Planetary gamma-ray spectroscopy, in *Proc. Lunar Planet. Sci. Conf. 9th* (1978), pp. 2961

H. Takeda et al., Magnesian anorthosites and a deep crustal rock from the farside crust of the Moon. Earth Planet. Sci. Lett. **247**, 171 (2006)

S.R. Taylor, G.J. Taylor, L.A. Taylor, The Moon: A Taylor perspective. Geochim. Cosmochim. Acta **70**, 5904 (2006)

J. Valentine (ed.), *The 2007 Recommendations of the International Commission on Radiological Protection*, vol. 37 (2007), p. 266

P.H. Warren, "New" lunar meteorites: Implications for composition of the global lunar surface, lunar crust, and the bulk Moon. Meteor. Planet Sci. **40**, 477 (2005)

P. Wessel, W.H.F. Smith, Free software helps map and displaydata. EOS Trans. AGU **72**, 441 (1991)

D. York, Least-squares fitting of a straight line. Can. J. Phys. **44**, 1079 (1966)

D. York, Least squares fitting of a straight line with correlated errors. Earth Planet. Sci. Lett. **5**, 320 (1969)